



HAL
open science

Automated analysis of human cochlea shape variability from segmented μ CT images

Thomas Demarcy, Clair Vandersteen, Nicolas Guevara, Charles Raffaelli, Dan Gnansia, Nicholas Ayache, Hervé Delingette

► **To cite this version:**

Thomas Demarcy, Clair Vandersteen, Nicolas Guevara, Charles Raffaelli, Dan Gnansia, et al.. Automated analysis of human cochlea shape variability from segmented μ CT images. *Computerized Medical Imaging and Graphics*, 2017, 59 (July 2017), pp.1 - 12. 10.1016/j.compmedimag.2017.04.002 . hal-01528489

HAL Id: hal-01528489

<https://inria.hal.science/hal-01528489>

Submitted on 29 May 2017

HAL is a multi-disciplinary open access archive for the deposit and dissemination of scientific research documents, whether they are published or not. The documents may come from teaching and research institutions in France or abroad, or from public or private research centers.

L'archive ouverte pluridisciplinaire **HAL**, est destinée au dépôt et à la diffusion de documents scientifiques de niveau recherche, publiés ou non, émanant des établissements d'enseignement et de recherche français ou étrangers, des laboratoires publics ou privés.

Automated Analysis of Human Cochlea Shape Variability from segmented μ CT images

Thomas Demarcy^{a,b,*}, Clair Vandersteen^{a,c}, Nicolas Guevara^c, Charles Raffaelli^d, Dan Gnansia^b,
Nicholas Ayache^a, Hervé Delingette^a

^a*Asclepios Research Team, Inria Sophia Antipolis-Méditerranée, France*

^b*Department of Cochlear Implant Scientific Research, Oticon Medical, France*

^c*Head and Neck University Institute (IUF), Nice, France*

^d*ENT Imaging Department, Nice University Hospital (CHU), France*

Abstract

The aim of this study is to define an automated and reproducible framework for cochlear anatomical analysis from high-resolution segmented images and to provide a comprehensive and objective shape variability study suitable for cochlear implant design and surgery planning. For the scala tympani (ST), the scala vestibuli (SV) and the whole cochlea, the variability of the arc lengths and the radial and longitudinal components of the lateral, central and modiolar paths are studied. The robustness of the automated cochlear coordinate system estimation is validated with synthetic and real data. Cochlear cross-sections are statistically analyzed using area, height and width measurements. The cross-section tilt angle is objectively measured and this data documents a significant feature for occurrence of surgical trauma.

Keywords: cochlear implant, human cochlea, anatomy, shape variability, modiolar axis

1. Introduction

The human cochlea is a spiral-shaped structure located in the inner ear. Essential organ of audition, its largest diameter is about 8.5 mm at the basal turn and its height about 7 mm (Dimopoulos and Muren, 1990). Cochlear structures include three scalae (or ducts) with complex morphology and showing interindividual variability in size and shape.

Cochlear implant surgery is an effective treatment for severe to profound sensorineural hearing loss. The classical implantation procedure involves drilling a path through the mastoid in order to reach the tympanic cavity allowing the surgeon to open the scala tympani (one of the three cochlear ducts) and insert an electrode array. The functional outcomes for these subjects are linked to the potential insertion traumas (Aschendorff et al., 2007; Finley et al., 2008). The

insertion can lead to lesions of the modiolar, osseous spiral lamina or basilar membrane, resulting in degeneration of the ciliated (Adunka et al., 2004) and spiral ganglion cells (Leake et al., 1999). Because the viability of these cells is correlated with neuronal survival (Nadol, 1997) and speech expression (Xu et al., 2012; Fayad and Linthicum, 2006), it is crucial to avoid destroying them during surgery and to minimize injury to the previously cited anatomic structures with so-called atraumatic surgery techniques (James et al., 2005).

An improved knowledge of the cochlea shape variability is not only essential for diagnosis of shape abnormality, atraumatic surgery planning and post-operative insertion assessment but it also provides a better anatomical understanding for the clinicians and can suggest electrode array design improvements

for cochlear implant manufacturers.

Various methods have been used for the analysis of human cochlear anatomical structures. Methods using several type of plastic casts have been widely employed to evaluate the dimensions of cochlear anatomy (Zrunek et al., 1980; Zrunek and Lischka, 1981; Dimopoulos and Muren, 1990; Hatsushika et al., 1990; Wysocki, 1999; Erixon et al., 2009; Rask-Andersen et al., 2011), but they do not allow accurate preservation of the geometric relationships of fragile cochlear structures and artifact-free measurements. Microdissections enable measurements of basic external dimensions of the cochlea like the width of the cochlear base (Wright and Roland, 2005), but as plastic casts, it cannot provide detailed three-dimensional reconstruction.

Histological sections offer the best image resolutions for the examination of fine cochlear structure (Hardy, 1938; Gulya and Steenerson, 1996; Biedron et al., 2010; Makary et al., 2010). However just as plastic casts and microdissection it is a destructive method. Indeed, the method needs several chemical steps such as dehydration, decalcification, fixation and staining, which may induce some tissue distortion and shrinkage (Buytaert et al., 2011; Rau et al., 2013).

Medical imaging techniques provide nondestructive methods. CT and MRI are common preoperative procedures. For the purpose of cochlear anatomy analysis, CT provides more information and even though MRI could be a complementary imaging modality (Thorne et al., 1999; Gibson et al., 2012), most of the studies published to date have focused on CT (Skinner et al., 2002; Escudé et al., 2006; Baker, 2008; van der Marel et al., 2014). However, conventional CT scan gives rather poor image resolution with respect to the cochlear dimensions.

As important cochlear anatomical structures such as the basilar membrane are not visible in CT imaging, analyses of the cochlea are commonly performed using μ CT images (Verbist et al., 2009; Poznyakovskiy et al., 2011; Gunz et al., 2012; Shin et al., 2013; Avci et al., 2014; Ceresa et al., 2014). In order to improve contrast, temporal bone samples can be fixed and stained before imaging (Poznyakovskiy

et al., 2011). Cochlear fluids are commonly removed (Postnov et al., 2006; Poznyakovskiy et al., 2011; Avci et al., 2014; Ceresa et al., 2014) but this operation requires to drill through the round and oval windows and to replace the perilymph with air by suction. The influence of this method on the geometry of the membranous structures is unknown (Rau et al., 2013) and μ CT scanning with fluid removal cannot be considered as nondestructive.

Previous analyses include measurements of the length of the cochlea and the number of cochlear turns (Hardy, 1938; Kawano et al., 1996; Skinner et al., 2002; Escudé et al., 2006; Stakhovskaya et al., 2007; Erixon et al., 2009; Gunz et al., 2012; Shin et al., 2013; van der Marel et al., 2014), measurements of the heights, widths and sectional areas of the scala tympani (Zrunek et al., 1980; Zrunek and Lischka, 1981; Hatsushika et al., 1990; Gulya and Steenerson, 1996; Wysocki, 1999; Thorne et al., 1999; Biedron et al., 2010; Avci et al., 2014), the scala vestibuli (Zrunek and Lischka, 1981; Gulya and Steenerson, 1996; Wysocki, 1999; Thorne et al., 1999; Biedron et al., 2010) and the cochlea (Erixon et al., 2009; Shin et al., 2013), measurements of the radial component of the cochlear centerlines (also called cochlear curvature) (Cohen et al., 1996; Baker, 2008; van der Marel et al., 2014), and studies of the longitudinal component of the centerlines of the scala tympani (Avci et al., 2014) and the cochlea itself (Verbist et al., 2009).

In this article, the variability of the human cochlea was studied from nine μ CT scans with a nondestructive preparation technique. The anatomical study provides a comprehensive set of measurements on the basis of new methods, which avoid inter-expert variability of manual measurements and can cope with the presence of noise and outliers. The central path analysis includes not only measurements of the scala tympani but also of the scala vestibuli and the whole cochlea, including lateral and modiolar paths. The centerlines were extracted with an image processing pipeline and expressed in a non-ambiguous cylindrical “cochlear” coordinate system, estimated with an original robust method. From the centerlines, cross-sections of the tympanic and vestibular ducts were

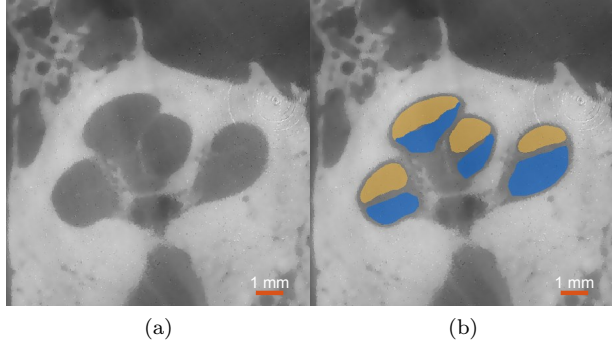


Figure 1: (a) μ CT image acquired on patient #4. An anisotropic diffusion filter was applied to reduce image noise. (b) Segmentations of the scala tympani (blue) and the scala vestibuli (yellow). The round window is not present in this slice.

acquired in a new non-ambiguous moving frame. The heights, widths, areas and their respective variability across the nine samples, were estimated along the centerline. The cross-section tilt angle was for the first time quantified.

2. Materials and methods

2.1. Nondestructive preparation of human cochleae

Nine healthy human temporal bones (5 right and 4 left sides) were obtained from cadavers harvested within 24 hours after death. An otologic surgeon harvested the entire temporal bone keeping intact the mastoid, the tympanic cavity and cochlear fluids in order to prevent any damage of the membranous structures. Using an *in vivo* high-resolution μ CT scanner (GE eXplore speCZT system), μ CT images with isotropic voxel size of $24.79 \mu\text{m}$ were acquired. Unlike previous studies no destructive preparation techniques, such as cochlear fluids removal, were performed. The contrast level was, however, sufficient to perform manual segmentation (Fig. 1 and 2).

2.2. Interactive segmentation

Automatic segmentation of the cochlear structures has been widely studied over the last decade (Xianfen et al., 2005; Schuman et al., 2010; Noble et al., 2011;

Reda et al., 2013, 2014a,b; Franz et al., 2014). Image segmentation is not the main focus of this study but a prerequisite for the shape analysis of delineated structures.

The μ CT images were cropped around the inner ear region. In order to improve the quality of the images before segmentation an anisotropic diffusion filter (Perona and Malik, 1990) was applied (Fig. 1a), which denoise the image while preserving edge contrast. Histogram equalization was then performed to enhance the contrast of the images. Each image was segmented using the interactive semi automated tool GeoS (Criminisi et al., 2008) by a head and neck imaging expert (Fig. 1b). The image resolution is high enough to identify the basilar membrane but insufficient to identify the Reissner's membrane and distinguish the scala media (or cochlear duct) from

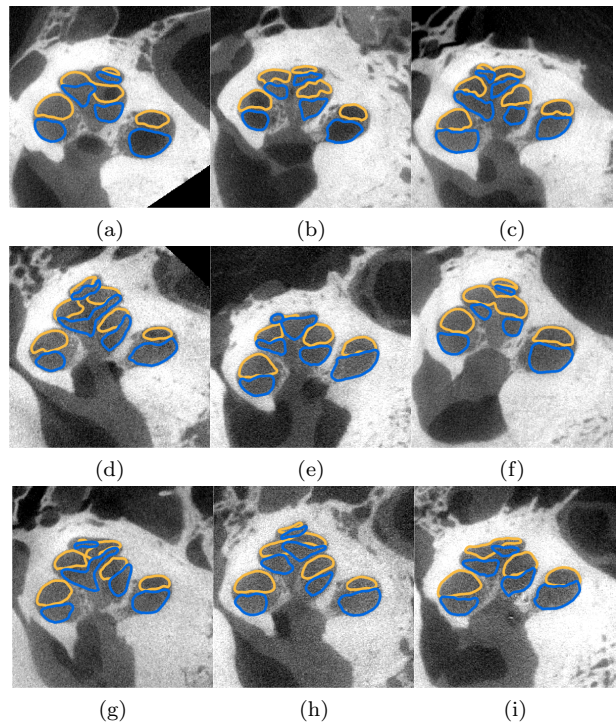


Figure 2: CT images of the nine segmented cochleae. Manually segmented tympanic (blue) and vestibular (yellow) ducts are presented in the yz -plane (see Fig. 5).

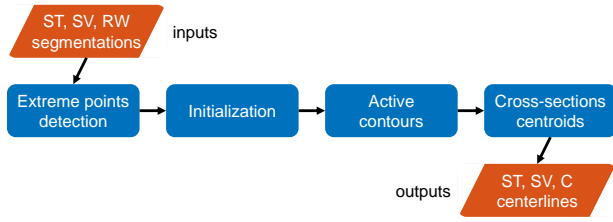


Figure 3: Flowchart of the automated centerline extraction. (Abbreviations: ST, scala tympani; SV, scala vestibuli; RW, round window; C, cochlea).

the scala vestibuli. The first segmented area corresponds to the round window, the second to the scala tympani and the third to the scala vestibuli, the scala media and the semi-circular canals taken together. Here we focused on the anatomy of the cochlea, discarding the vestibule. Henceforth, unless otherwise specified, the label “scala vestibuli” refers to both vestibular and cochlear ducts (as frequently in other studies (Gulya and Steenerson, 1996; Wysocki, 1999; Yoo et al., 2000a; Postnov et al., 2006; Meshik et al., 2010; Noble et al., 2011; Braun et al., 2012)). Fig. 2 presents the nine segmented μ CT images.

2.3. Automated centerline extraction

The challenge of cochlear centerline extraction has already been dealt with (Baker and Barnes, 2004; Verbist et al., 2009; Poznyakovskiy et al., 2011; Gunz et al., 2012). A flowchart of the method applied in this study and the results are respectively given on Fig. 3 and Fig. 4. We performed a standard active contours approach (Kass et al., 1988) driven by the signed distance function which determines the distance of a given point from the shape boundary of the segmented anatomical structure. The method is followed by an adjustment using cross-section centroids to ensure that the centerline is properly centered. For the full explanation of the series of algorithm used for automated centerline extraction the reader is referred to the Appendix A in the supplementary materials.

2.4. Robust modiolar axis estimation

The cochlear coordinate system (x, y, z) by Verbist et al. (2010) provide a standard and unambiguous framework for anatomic studies of the cochlea.

It can be defined independently from a modality-centered anatomical coordinate system. The modiolus is a cone-shape bony structure around which the first two turns of the cochlea are wrapped. The z -axis is chosen as the modiolar-axis. As Verbist et al. (2010) point out, there exist two main alternatives for the origin: the helicotrema (at the apex) with the z -axis oriented from the apex to the base of the modiolus, or the base with the reversed orientation. To remove any ambiguity, we call the former option “apical cochlear coordinate system” (ACCS) (Verbist et al., 2010) and the latter “basal cochlear coordinate system” (BCCS) (see Fig. 5). In both coordinate systems, the xz -plane passes through the center of the round window, x values being positive at the level of the round window. The y -axis is set in order to have $(\hat{x}, \hat{y}, \hat{z})$ being an orthonormal basis. In this study we chose the BCCS. A flowchart of the methods used for anatomical analysis of the cochlea is given on Fig. 6.

One of the major difficulties is to define the modiolar axis. Most of previous studies define this axis by manually adjusted multiplanar reconstruc-

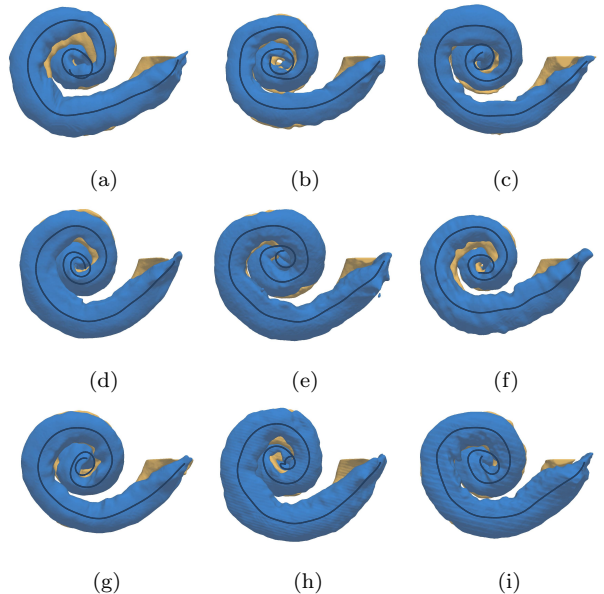


Figure 4: Nine ST centerlines overlaid over their corresponding three-dimensional segmented cochleae.

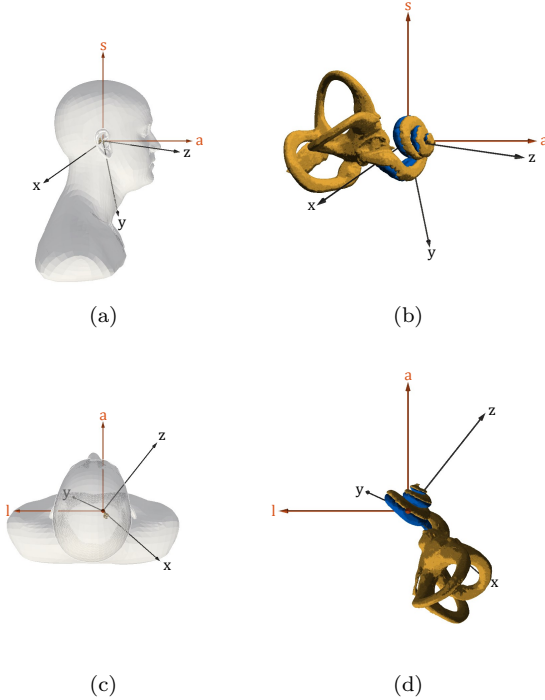


Figure 5: Comparison of modality-centered anatomical coordinate system (l, a, s) and BCCS (x, y, z) . (a) Left sagittal view from posterior to anterior (a -axis) and from inferior to superior (s -axis) and (b) its corresponding close-up view. (c) Superior transverse view from left (l -axis) to right and from posterior to anterior (a -axis) and (d) its corresponding close-up view. The segmented scala tympani (blue) and the bony labyrinth (yellow) of the patient #1 (right cochlea) are represented. The z -axis oriented from the base to the apex of the modiolus, the x -axis passes through the center of the round window. There is no simple relationship (such as coplanarity) between axes and planes from the two coordinate systems. The angle between a and z -axes is known to be around 45° (Xu et al., 2000), which is not exactly the case here.

tion (Baker, 2008; van der Marel et al., 2014) or simply by setting manually two points (Poznyakovskiy et al., 2008; Verbist et al., 2009; Kjer et al., 2015). Escudé et al. (2006) proposed maximization of dark pixel area using minimum intensity projection. Yoo et al. (2000b) determined the modiolar axis using three nonlinear least square minimization based algorithms. Misalignment of the modiolar axis may greatly impact the measurements and can be a cause

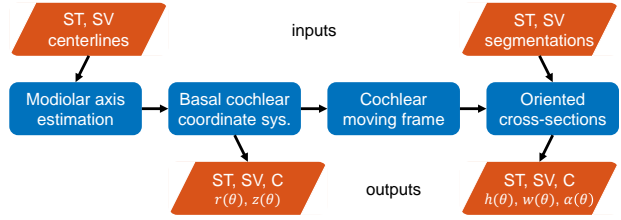


Figure 6: Flowchart of the shape parametrization. The centerline is derived in its radial $r(\theta)$ and longitudinal $z(\theta)$ components in a cylindrical coordinate system called BCCS. The cross-sections are expressed in a cochlear moving frame allowing for measurements of their heights $h(\theta)$, widths $w(\theta)$ and tilt angles $\alpha(\theta)$. (Abbreviations: ST, scala tympani; SV, scala vestibuli; C, cochlea).

of non reproducibility of the results.

Helico-spiral axis inference. The challenge is to estimate the unknown modiolar axis $\hat{\mathbf{z}}$ from the cochlear centerline \mathbf{x} expressed in another coordinate system. We propose a method based on the intrinsic geometrical properties of the centerlines, more specifically based on the locus of the centers of curvature of the centerline.

The cochlear centerline is most frequently described as a logarithmic spiral (Cohen et al., 1996; Xu et al., 2000; Yoo et al., 2000a,b; Baker, 2008). In a cylindrical coordinate system (where $(\hat{\mathbf{r}}, \hat{\boldsymbol{\theta}}, \hat{\mathbf{z}})$ are the local radial, circumferential and longitudinal unit vectors) an ideal logarithmic helico-spiral can be written as:

$$\mathbf{x} = ae^{-b\theta}\hat{\mathbf{r}} + c\theta\hat{\mathbf{z}} \quad (1)$$

where a , b and c are positive constants. This cochlear model, completely parameterized by $\theta \in [\theta_0, \theta_1]$, is close to the one given by Clark et al. (2011), discarding the piecewise definition of the radial function used to model the basal turn.

The radial and longitudinal components of \mathbf{x} are:

$$r(\theta) = ae^{-b\theta} \quad (2)$$

$$z(\theta) = c\theta. \quad (3)$$

Let us consider an infinitesimal part of the curve in the cylindrical coordinate system

Table 1: Logarithmic helico-spiral constants for cochlear model. The values for the constants are given by Clark et al. (2011).

a (mm)	b (rad ⁻¹)	c (mm·rad ⁻¹)	θ_0 (rad)	θ_1 (rad)
3.762	0.07546	0.1751	0	15.71

$$ds^2 = dr^2(\theta) + r^2(\theta)d\theta^2 + dz^2(\theta) \quad (4)$$

$$ds^2 = b^2r^2(\theta)d\theta^2 + r^2(\theta)d\theta^2 + c^2d\theta^2 \quad (5)$$

$$ds = \sqrt{(b^2 + 1)r^2(\theta) + c^2}d\theta. \quad (6)$$

We assume that $c^2 \ll r(\theta)^2 \forall \theta \in [\theta_0, \theta_1]$ since, in practice, using the values in table 1,

$$\begin{aligned} 2.2 \times 10^{-3} &\approx \frac{c^2}{r(\theta_0)^2} \leq \frac{c^2}{r(\theta)^2} \\ &\leq \frac{c^2}{r(\theta_1)^2} \approx 2.3 \times 10^{-2} \end{aligned} \quad (7)$$

We define differential arc length $d\tilde{s}$ as follows,

$$d\tilde{s} = \sqrt{b^2 + 1}r(\theta)d\theta \quad (8)$$

Let us define the function γ and ϵ ,

$$\begin{aligned} \gamma &= \frac{d\tilde{s}}{ds} = \frac{\sqrt{b^2 + 1}r(\theta)}{\sqrt{(b^2 + 1)r^2(\theta) + c^2}} \\ &= 1 - \frac{c^2}{2(b^2 + 1)r^2(\theta)} + o\left(\frac{c^2}{r^2(\theta)}\right) \approx 1 \end{aligned} \quad (9)$$

$$\begin{aligned} \epsilon &= \left| \frac{d^2\tilde{s}}{ds^2} \right| = \left| \frac{d}{ds} \left(\frac{d\tilde{s}}{ds} \right) \right| \\ &= \frac{\sqrt{b^2 + 1}br(\theta)c^2}{\left((b^2 + 1)^2 r^2(\theta) + c^2 \right)^2} \propto \frac{c^2}{r^3(\theta)} \ll 1. \end{aligned} \quad (10)$$

The tangent unit vector $\hat{\mathbf{t}}$ is defined as:

$$\hat{\mathbf{t}} = \frac{d\mathbf{x}}{ds} = \frac{d\mathbf{x}}{d\tilde{s}} \frac{d\tilde{s}}{ds} = \frac{-br(\theta)\hat{\mathbf{r}} + r(\theta)\hat{\boldsymbol{\theta}} + c\hat{\mathbf{z}}}{\sqrt{b^2 + 1}r(\theta)}\gamma \quad (11)$$

$$\begin{aligned} \kappa\hat{\mathbf{n}} &= \frac{d\hat{\mathbf{t}}}{ds} = \frac{d^2\mathbf{x}}{ds^2} = \frac{d}{ds} \left(\frac{d\mathbf{x}}{d\tilde{s}} \frac{d\tilde{s}}{ds} \right) \\ &= \frac{d^2\mathbf{x}}{d\tilde{s}^2} \left(\frac{d\tilde{s}}{ds} \right)^2 + \frac{d\mathbf{x}}{d\tilde{s}} \frac{d^2\tilde{s}}{ds^2} = \frac{d^2\mathbf{x}}{d\tilde{s}^2} \gamma^2 - \frac{d\mathbf{x}}{d\tilde{s}} \epsilon \end{aligned} \quad (12)$$

where κ is the curvature and $\hat{\mathbf{n}}$ is the normal unit vector. Using the approximations of γ and ϵ ,

$$\kappa\hat{\mathbf{n}} \approx \frac{d^2\mathbf{x}}{d\tilde{s}^2} = \frac{-r(\theta)\hat{\mathbf{r}} - br(\theta)\hat{\boldsymbol{\theta}} + bc\hat{\mathbf{z}}}{(b^2 + 1)r^2(\theta)} \quad (13)$$

$$\begin{aligned} \kappa^2 &= \|\kappa\hat{\mathbf{n}}\|^2 \approx \frac{(b^2 + 1)r^2(\theta) + b^2c^2}{\left((b^2 + 1)^2 r^2(\theta) \right)^2} \\ &\approx \frac{1}{(b^2 + 1)r^2(\theta)} + \frac{b^2c^2}{\left((b^2 + 1)^2 r^2(\theta) \right)^2} \end{aligned} \quad (14)$$

where the second term in the right-hand side equation ($\propto c^2/r^4(\theta)$) can be neglected, the curvature is then,

$$\kappa \approx \frac{1}{\sqrt{b^2 + 1}r(\theta)}. \quad (15)$$

We can now approximate the following terms,

$$\frac{\hat{\mathbf{t}}}{\kappa} \approx -br(\theta)\hat{\mathbf{r}} + r(\theta)\hat{\boldsymbol{\theta}} + c\hat{\mathbf{z}} \quad (16)$$

$$\frac{\hat{\mathbf{n}}}{\kappa} \approx -r(\theta)\hat{\mathbf{r}} - br(\theta)\hat{\boldsymbol{\theta}} + bc\hat{\mathbf{z}}. \quad (17)$$

The evolute \mathbf{e} of curve \mathbf{x} is the locus of all its centers of curvature, the evolute of an logarithmic helico-spiral has the parametric equation:

$$\mathbf{e} = \mathbf{x} + \frac{\hat{\mathbf{n}}}{\kappa} \approx -br(\theta)\hat{\boldsymbol{\theta}} + c \cdot (\theta + b)\hat{\mathbf{z}}. \quad (18)$$

We propose to build a corrected evolute \mathbf{e}_c which is a sole function of the modiolar axis enabling to remove the circumferential dependency,

$$\begin{aligned} \mathbf{e}_c &= \mathbf{x} + \frac{b}{1+b^2} \frac{\hat{\mathbf{t}}}{\kappa} + \frac{1}{1+b^2} \frac{\hat{\mathbf{n}}}{\kappa} \\ &\approx c \cdot \left(\theta + \frac{2b}{1+b^2} \right) \hat{\mathbf{z}}. \end{aligned} \quad (19)$$

The corrected evolute estimates the modiolar axis, aligned with $\hat{\mathbf{z}}$, using only the intrinsic geometrical properties of the cochlear centerline, the curve \mathbf{x} i.e. its position, its local tangent and normal unit vector $\hat{\mathbf{t}}$ and $\hat{\mathbf{n}}$, its local curvature κ , and a constant parameter b . The result is independent from the modality-centered coordinate system (defined in the axial, coronal and sagittal planes).

The parameter b is a widely studied cochlear measurement, here it was set to the optimum value found by Cohen et al. (1996) among 30 patients ($b = 0.075 \text{ rad}^{-1}$).

Robust Principal Component Analysis (PCA). The modiolar axis is thus computed from the cochlear centerline as the locus of the corrected evolute. In practice, discretization errors (see Appendix B for more details) and model errors (the centerline may not be a perfect logarithmic spiral) cause the discrete corrected evolute points to lie close to the modiolar axis but not exactly on it. Thus it is necessary to estimate the line which best approximates the discrete corrected evolute in a robust manner in order to cope with the presence of noise and outliers. This is equivalent to performing robust PCA as we are looking for the first principle component of the cloud of points. Robust PCA is performed using an extension of the expectation maximization (EM) algorithm called ECME (Liu and Rubin, 1995) fitting Student’s t -distributions instead of Gaussian distributions. The Student’s t -distribution can be interpreted as an infinite weighted sum of normal distributions with the same mean and variance determined by a gamma distribution. In the Maximization step the mean and the variance are updated by computing a weighted sum of the data.

In the cylindrical coordinate system (r, θ, z) constructed from the BCCS (x, y, z) , the radial component $r(\theta)$ and the longitudinal component $z(\theta)$ of

the centerlines were extracted for the tympanic and vestibular ducts and the cochlea.

2.5. Cochlear moving frame

In order to evaluate the internal dimensions of the cochlea, cross-section measurements were performed in radial planes (a.k.a mid-modiolar cross-sections) (Zrunek et al., 1980; Zrunek and Lischka, 1981; Erixon et al., 2009), in parallel planes such as histological sections (Biedron et al., 2010) and in planes normal to the centerline (Poznyakovskiy et al., 2011; Avci et al., 2014). This last method does not induce measurement errors (e.g. the section of a circular cylinder performed in plane not normal to the axis produces an ellipse).

Planes normal to the centerline can be defined in the Frenet-Serret moving frame (where $(\hat{\mathbf{t}}, \hat{\mathbf{n}}, \hat{\mathbf{b}})$ are the basis vectors). This coordinate system is traditionally used for centerline-based cochlear models (Viergever, 1978), however, its moving frame presents the significant drawback that the binormal unit vector may be ill-defined at inflection points (see Fig. 8a). Instead, to overcome this drawback, let us define the vectors:

$$\hat{\mathbf{u}} = \frac{\hat{\mathbf{z}} \times \hat{\mathbf{t}}}{\|\hat{\mathbf{z}} \times \hat{\mathbf{t}}\|} \quad (\text{a}) \quad \hat{\mathbf{v}} = \hat{\mathbf{t}} \times \hat{\mathbf{u}} \quad (\text{b}) \quad (20)$$

where $\hat{\mathbf{z}}$ is the unit vector of modiolar axis, $\hat{\mathbf{t}}$ is the unit vector tangent to the centerline and the symbol \times denotes the cross product. $(\hat{\mathbf{t}}, \hat{\mathbf{u}}, \hat{\mathbf{v}})$ defines a moving frame which is always well defined because $\hat{\mathbf{t}}$ (and $\hat{\mathbf{z}}$) is never degenerated (see Fig. 8b). The cross-sectional measurements can then be performed locally in the uv -planes.

Oriented cross-sections. Along the cochlear centerline the cross-sections of the scalae tympani and vestibuli were acquired in the normal uv -planes. The cross-sections may have problems with accuracy at the two extremities of the centerline. Near the round window the cross-sections of the label “scala vestibuli” can leak into the vestibule as well as the cross-sections may not be perfectly defined at the apical turn since both scalae are supposed to merge

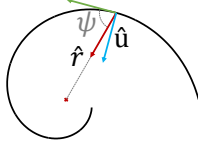


Figure 7: $\hat{\mathbf{u}}$ and $\hat{\mathbf{v}}$ can be linked to the radial $r(\theta)$ and longitudinal component $z(\theta)$ of the central paths. $\hat{\mathbf{u}}$ is defined in the xy -plane and $\angle\hat{\mathbf{u}}\hat{\mathbf{r}}$ the angle between $\hat{\mathbf{u}}$ and $\hat{\mathbf{r}}$, the radial unit vector, is the complementary to the logarithmic spiral pitch $\psi = \cot^{-1}(b)$ where b is constant for a logarithmic spiral (a.k.a. equiangular spiral) (as in Eq. 1). $\angle\hat{\mathbf{v}}\hat{\mathbf{z}}$ the angle between $\hat{\mathbf{v}}$ and $\hat{\mathbf{z}}$, is the longitudinal growth rate, $\angle\hat{\mathbf{v}}\hat{\mathbf{z}}(\theta) = \arctan(dz/d\theta)$.

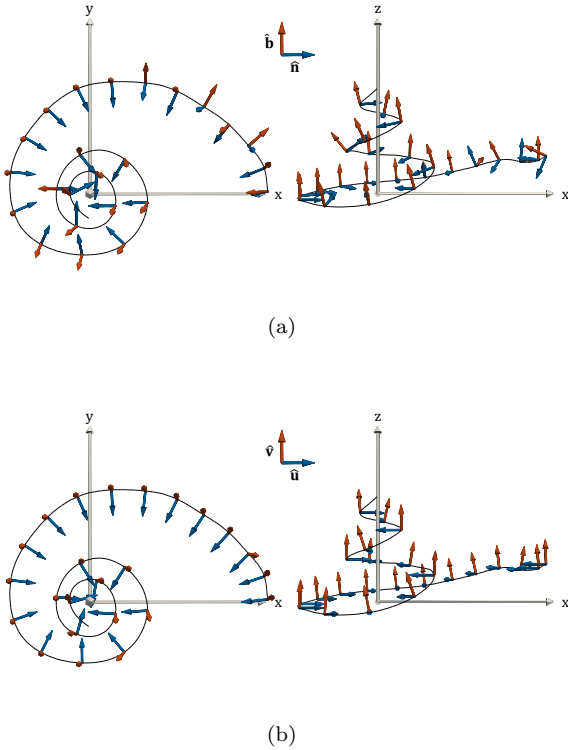


Figure 8: (a) Frenet-Serret frame. The start of the first basal turn is known to be not perfectly logarithmic (Cohen et al., 1996) and can present inflection points. Here the normal unit vector $\hat{\mathbf{n}}$ (blue) and the binormal unit vector $\hat{\mathbf{b}}$ (red) vary singularly, as we can see notably within first five represented moving frames. (b) New cochlear moving frame. The vectors $\hat{\mathbf{u}}$ (blue) and $\hat{\mathbf{v}}$ (red) vary smoothly along the centerline.

at the apex. Potential errors are detected with the change in the cross-sectional areas. An abrupt increase of one of the areas is indeed related to a leakage. The improper cross-sections were constrained to vary smoothly, by imposing incorrect cross-sections to be inside the morphological dilatation of their correct neighbor.

Cross-sections are fitted independently for each normal plane with ellipses using classical principal component analysis. The major axes define the widths of the ducts w_{ST} and w_{SV} and the minor axes define the heights of the ducts h_{ST} and h_{SV} . The ellipses also provide an orientation. Let us call α_{ST} (respectively α_{SV}) the angle between $\hat{\mathbf{u}}$ (i.e. the xy -plane) and the major axis of the scala tympani (respectively the scala vestibuli). The cochlear tilt angle α is defined as the mean of α_{ST} and α_{SV} (see Fig. 15b). Positive values of the tilt angle mean that locally the scala tympani is more lateral than the scala vestibuli and conversely for negative values (to be consistent with the profile tilt angles in (Clark et al., 2011)).

x_{lat}^{ST} (respectively x_{mod}^{ST}) that represents the set of points defining the paths along the tympanic lateral (respectively modiolar) walls can be computed from the tympanic centerline x^{ST} using the cross-section measurements.

$$x_{lat}^{ST}(s) = x^{ST}(s) - \frac{w_{ST}}{2}(\cos(\alpha_{ST})\hat{\mathbf{u}} - \sin(\alpha_{ST})\hat{\mathbf{v}}) \quad (21a)$$

$$x_{mod}^{ST}(s) = x^{ST}(s) + \frac{w_{ST}}{2}(\cos(\alpha_{ST})\hat{\mathbf{u}} - \sin(\alpha_{ST})\hat{\mathbf{v}}). \quad (21b)$$

These values can be computed similarly on the scala vestibuli.

3. Results

3.1. Centerlines measurements

Table 2 shows the variability of basic measurements determined from the individual cochlear centerlines. The number of cochlear turn is statistically

equal to 2.57 ± 0.28 (mean and ± 1 standard deviation), the length of the cochlear centerline is equal to $24.4 \text{ mm} \pm 1.0$. No significant correlation was found between these two measurements ($R^2 = 0.39$). Most of the variability occurs at the apical turn. Fig. 9a illustrates the arc length along the scala tympani following the central path (i.e. centerline), the lateral or modiolar walls. A projected representation of the automatically extracted lateral, central and modiolar paths of a scala tympani is shown in Fig. 9b.

Fig. 10a presents the individual radial component of the tympanic centerlines and Fig. 10b, the mean radial component of the two scalae and their union. In the first part of the basal turn the scala tympani is slightly more lateral than the scala vestibuli. The radial component after 180° are roughly the same following a logarithmic form. The standard deviation of the radial component of the cochlear centerline ($r(\theta)$) averaged over the patients and the angular coordinate θ (between 0 and 900°) is equal to 0.11 mm .

Fig. 10c demonstrates the individual longitudinal component of the tympanic centerlines and Fig. 10d, the mean longitudinal component of the two scalae and their union. The standard deviation of the cochlear longitudinal component of the cochlear centerline ($z(\theta)$) averaged over the patients and the angular coordinate θ (between 0 and 900°) is equal to 0.46 mm , which is more than four times the value obtained for the radial component.

3.2. Modiolar axis estimation

Automated vs. manual estimation. In order to compare the current method, four cochlear anatomy experts estimated the modiolar axis by manually setting two points, several times for each temporal bones.

Let us consider the modiolar axis as a line $L = \{\mathbf{p} + s\hat{\mathbf{z}} | s \in \mathbb{R}\}$, where $\hat{\mathbf{z}}$ is a unit vector. We evaluate respectively the angle of rotation and the distance between two axes L_i and L_j using,

$$d_r(L_i, L_j) = |\sin^{-1}(\|\hat{\mathbf{z}}_i \times \hat{\mathbf{z}}_j\|)| \in [0, \pi] \quad (22a)$$

$$d_t(L_i, L_j) = \left| \frac{\hat{\mathbf{z}}_i \times \hat{\mathbf{z}}_j}{\|\hat{\mathbf{z}}_i \times \hat{\mathbf{z}}_j\|} \cdot (\mathbf{p}_j - \mathbf{p}_i) \right| \geq 0 \quad (22b)$$

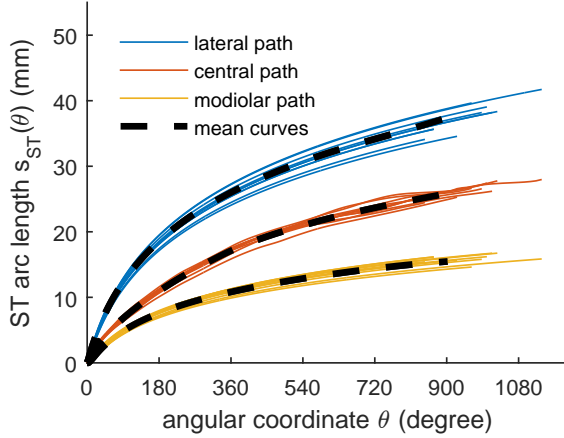
Table 2: Measurements determined from the individual cochlear centerlines

patient	cochlear turns	cochlear length (mm)	ST length (mm)	SV length (mm)
1	2.32	23.6	25.3	22.9
2	2.57	23.5	25.3	22.9
3	2.74	26.1	26.7	27.0
4	3.08	25.5	27.8	25.6
5	2.14	24.5	25.8	24.5
6	2.32	23.0	24.3	22.6
7	2.74	24.6	26.0	24.6
8	2.54	23.9	26.5	23.2
9	2.67	24.6	26.8	24.2

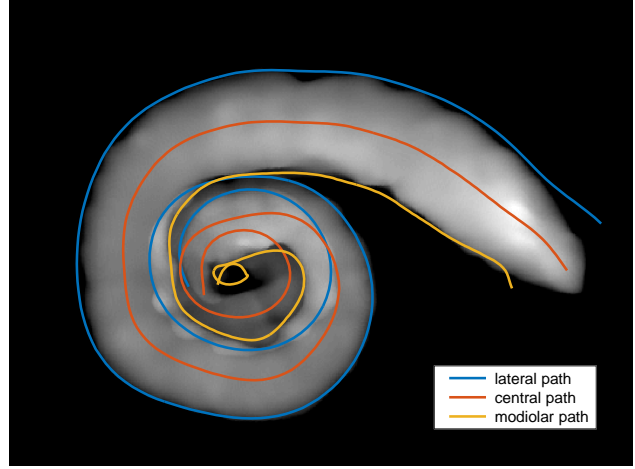
The inter- and intra-expert standard deviation equal respectively to 10.0° and 8.7° for the angle of rotation and 0.14 mm and 0.12 mm for the distance. The mean angle and distance between the automatically estimated and manually defined modiolar axis are respectively 10.2° and 0.28 mm . Fig. 11b shows an example of automatic and manual axis estimation.

Least square minimization method vs. evolute-based. Yoo et al. (2000b) designed two algorithms for the estimation of the modiolar axis from centerlines. Algorithm A utilized the longitudinal variation, while algorithm B considers the radial variation. They claimed that the former one is more accurate and suitable for three-dimensional data, which led us to implement it. Algorithm A is based on nonlinear optimization using steepest-descent algorithm and requires five parameters (μ_{A1} , TH_{A1} , μ_{A2} , TH_{A2} , C_{init}) whose values were not all specified in the article. We performed ourselves parameters tuning in order to get good results with the synthesized curves designed by the authors (summarized in Table 3).

The method described in subsection 2.4 is compared with the method introduced by Yoo et al. (2000b) using their own parametric model and angular sampling in order to perform a accurate com-



(a)



(b)

Figure 9: (a) Individual and mean arc length of the lateral, central and modiolar paths of the scala tympani as a function of the angular coordinate. Lateral, central and modiolar paths of a scala tympani (patient #2) projected into the xy -plane. The mean intensity projection of the segmentation is in the background.

Table 3: Parameters used to implement Yoo et al. (2000b)’s algorithm A

parameters	μ_{A1}	TH_{A1}	μ_{A2} (mm)	TH_{A2} (mm)	C_{init} (mm)
values	10^{-5}	10^{-5}	10^{-3}	10^{-3}	2.8

parison. Their centerline model is based on Fowler et al. (1992)’s model with a logarithmic spiral and an exponential term for the radial and the longitudinal component of the centerline. Fig. 12 shows the model for which the ideal axis is known.

Yoo et al. (2000b)’s method repeatedly updates the rotation parameters and the parameter C using the steepest-descent algorithm. The final rotation error depends on the initialization. The parameter C is an amplitude parameter that is used to model the longitudinal component of the helico-spiral. C depends on the (uniform) sampling (150 vertices for a total length of 35 mm). A criterion of convergence is that for each sampled point $i = 1, \dots, n$, C needs to be greater than difference between the adjacent longitudinal component $(\mathbf{x}_i - \mathbf{x}_{i-1}) \cdot \hat{\mathbf{z}}$. Fig. 13a shows

the rotation error with an optimized value of C_{init} (2.8 mm) but with different initial rotation around the x -axis (R_x), Yoo et al. (2000b) have tested the convexity of their objective function within a small orientation change (-10° to 10°), but in this study, μ CT images of the temporal bones are acquired in random orientations.

We evaluated the robustness of both methods by adding Gaussian noise to the original centerline. For every noise amplitude we generated 100 noisy centerlines and evaluated the mean rotation error. Since Yoo et al. (2000b)’s algorithm needs to be initialized, we used the most favorable conditions, i.e. the values in Table 3 with the initial rotation around the x and y -axis (R_x and R_y) equal to 45° and 0° and different C_{init} values. Our method is run only once since it does not depend on parameter C_{init} and it uses the Frenet-Serret formulas which are independent from the initial coordinate system. The mean errors are plotted in Fig. 13b.

We also estimated the distance (d_t) between the estimated modiolar axis and the ideal one, it is equal $0.005 \mu\text{m}$, which would represent 0.2 pixel on a μ CT image, while Yoo et al. (2000b) claimed 0 mm error.

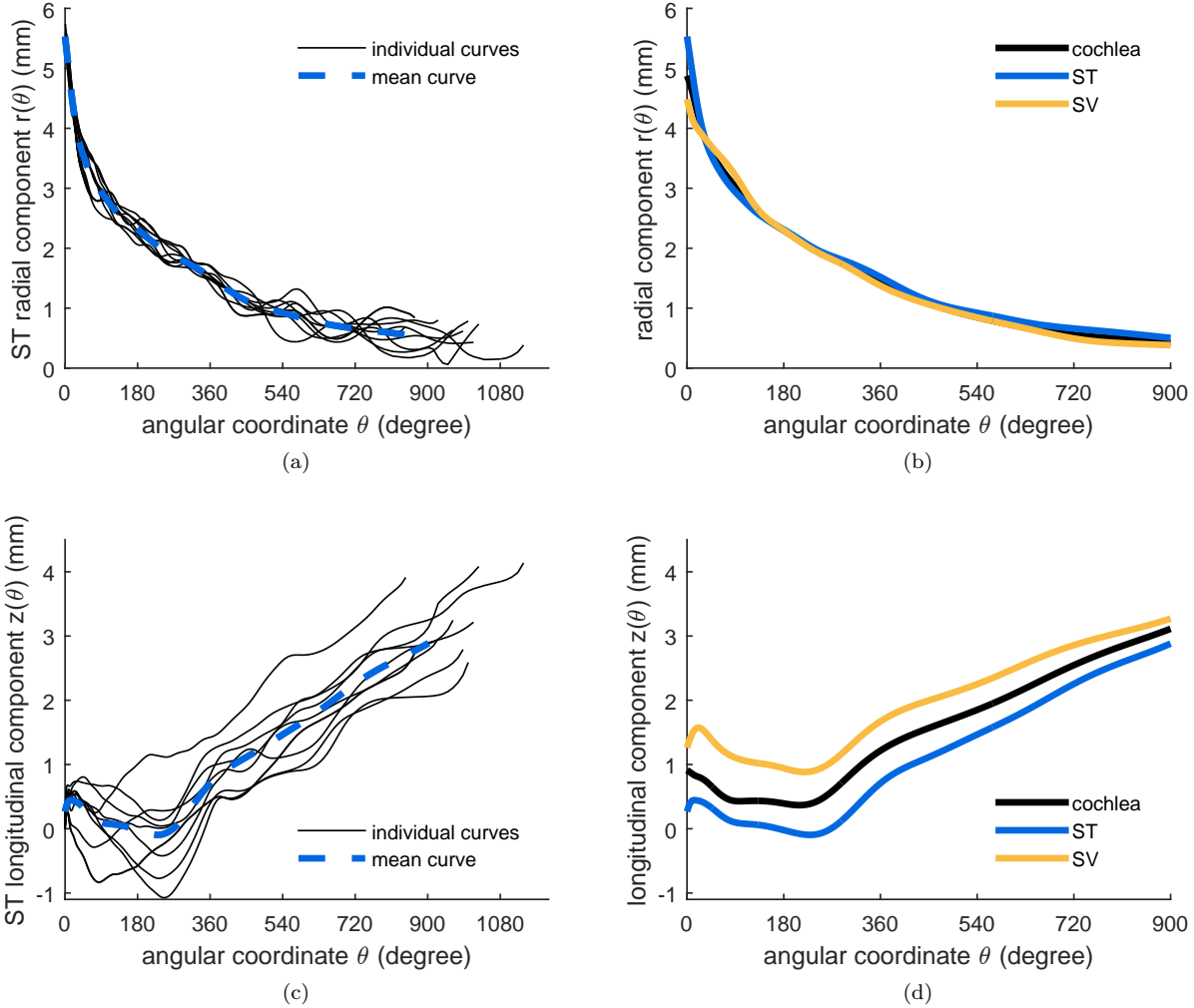


Figure 10: Individual and mean radial (a) and longitudinal (c) component of the tympanic centerline (ST); mean radial (b) and longitudinal (d) component of the tympanic (ST) and vestibular (SV) central paths as a function of the angular coordinate. The origin corresponds to the centers of the round windows.

Application to real data. Fig. 11a presents the method applied on real patient data, while Fig. 14 expresses the influence of the estimated modiolar axis on the radial and longitudinal components of the centerlines. With a rotation of the modiolar axis of 11.5° , the projected components can be significantly different. Avci et al. (2014) defined categories of the

longitudinal component of the tympanic centerline. Among other categories, the “rollercoaster” category was defined as a decreasing longitudinal component from the round window, changing to an increasing curve between 5 and 10 mm. The “sloping” category follows an increasing curve without any significant decreasing trends, local peaks located between

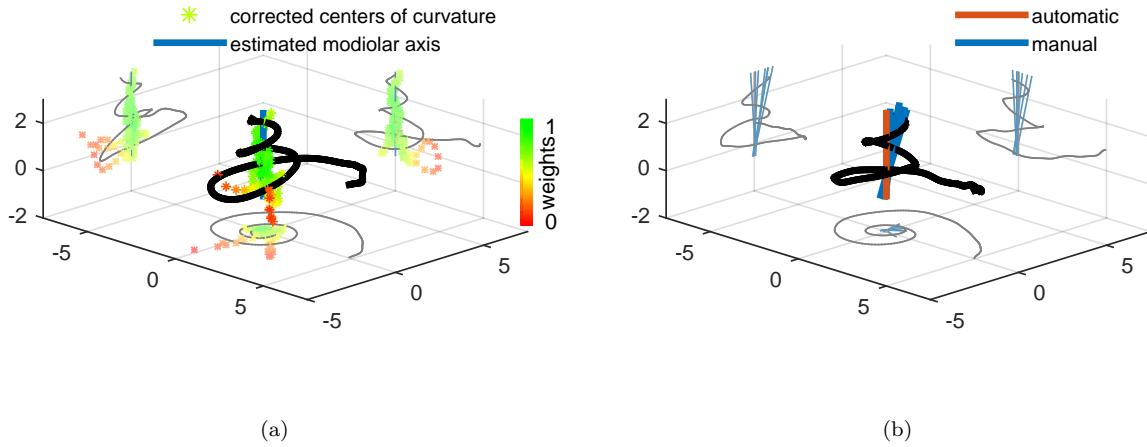


Figure 11: (a) Modiolar axis estimation from a real cochlear centerline (patient #3). A robust PCA of a multivariate Student’s t -distribution is performed on the corrected centers of curvature. The weights are shown with the color map, the green points are weighted more in the Student’s t -distribution whereas the red points belong to the tail of the distribution and are almost not taken into account. (b) Automatic and manual modiolar axis estimation from a real cochlear centerline (patient #1).

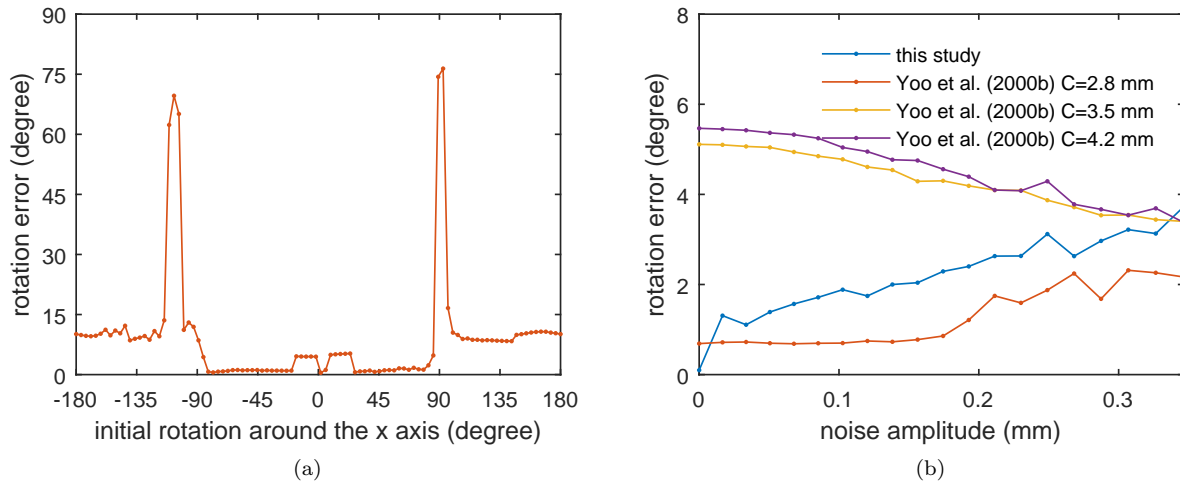


Figure 13: (a) Sensitivity of the algorithm A developed by Yoo et al. (2000b) with respect to the initial rotation R_x . (b) Noise sensitivity of the algorithm developed in this study and algorithm A developed by Yoo et al. (2000b) with different C_{init} values.

10 and 15 mm being also a feature of this category. Following this taxonomy, the estimated projection in Fig. 14b would have been classified as a “roller-

coaster” whereas the perturbed one appears more to correspond to the “sloping” category with a peak around 10 mm.

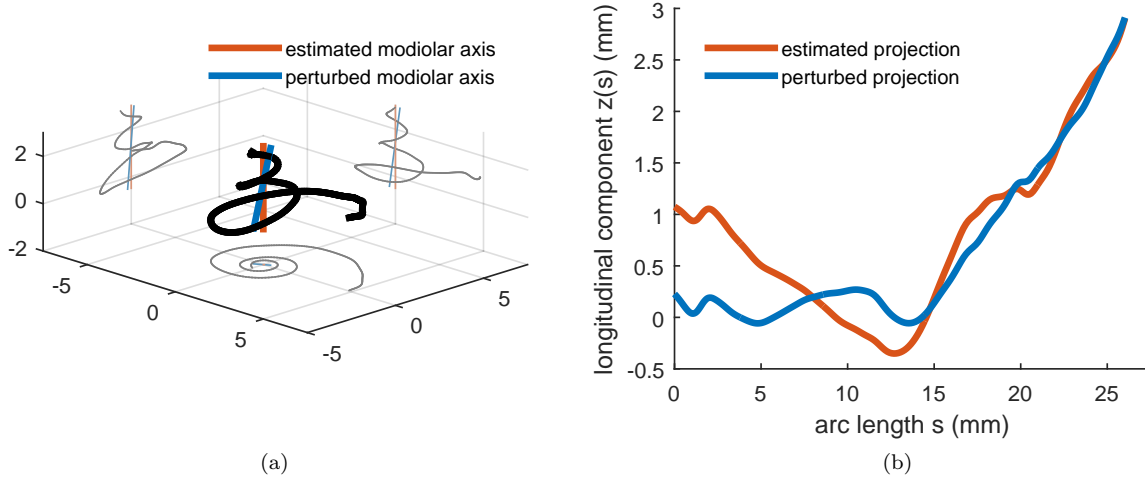


Figure 14: (a) Influence of the axis estimation on the centerline projected onto the modiolar axis (called longitudinal component). The angle between the original and the modified axis is equal to 11.5° . (b) Longitudinal component of the cochlear centerline as a function of the arc length. Both longitudinal components are extracted from the same cochlear centerline.

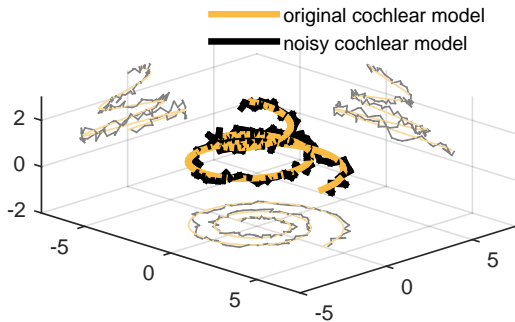


Figure 12: Synthetic cochlear model as defined by Yoo et al. (2000b) with and without random Gaussian noise at three different scale (0.23 mm, 0.94 mm, 3.76 mm) with a total amplitude of 0.18 mm.

3.3. Cross-sections measurements

Fig. 15 gives a sample of 24 cross-sections (represented in the uv -planes) computed from the three-dimensional segmentations.

Fig. 16 presents the mean cross-section area (Fig. 16b), height (Fig. 16c) and width (Fig. 16d) of the tympanic and vestibular ducts. After 360° the width of the scala tympani and vestibuli tend to be equal.

Fig. 16a presents the individual tilt angle α , the mean angle between $\hat{\mathbf{u}}$ and the major axes of the tympanic and vestibular scalae. Examples of the influence of the tilt angle can be appreciated in Fig. 15a, b and c.

4. Discussion

4.1. Parametrization framework

The distance along the cochlear central path s and its angular parametrization θ are both used in the literature. The distance can be measured from the different centerlines (scala tympani, scala vestibuli or the whole cochlea), which produces different parametrization (see the different final length

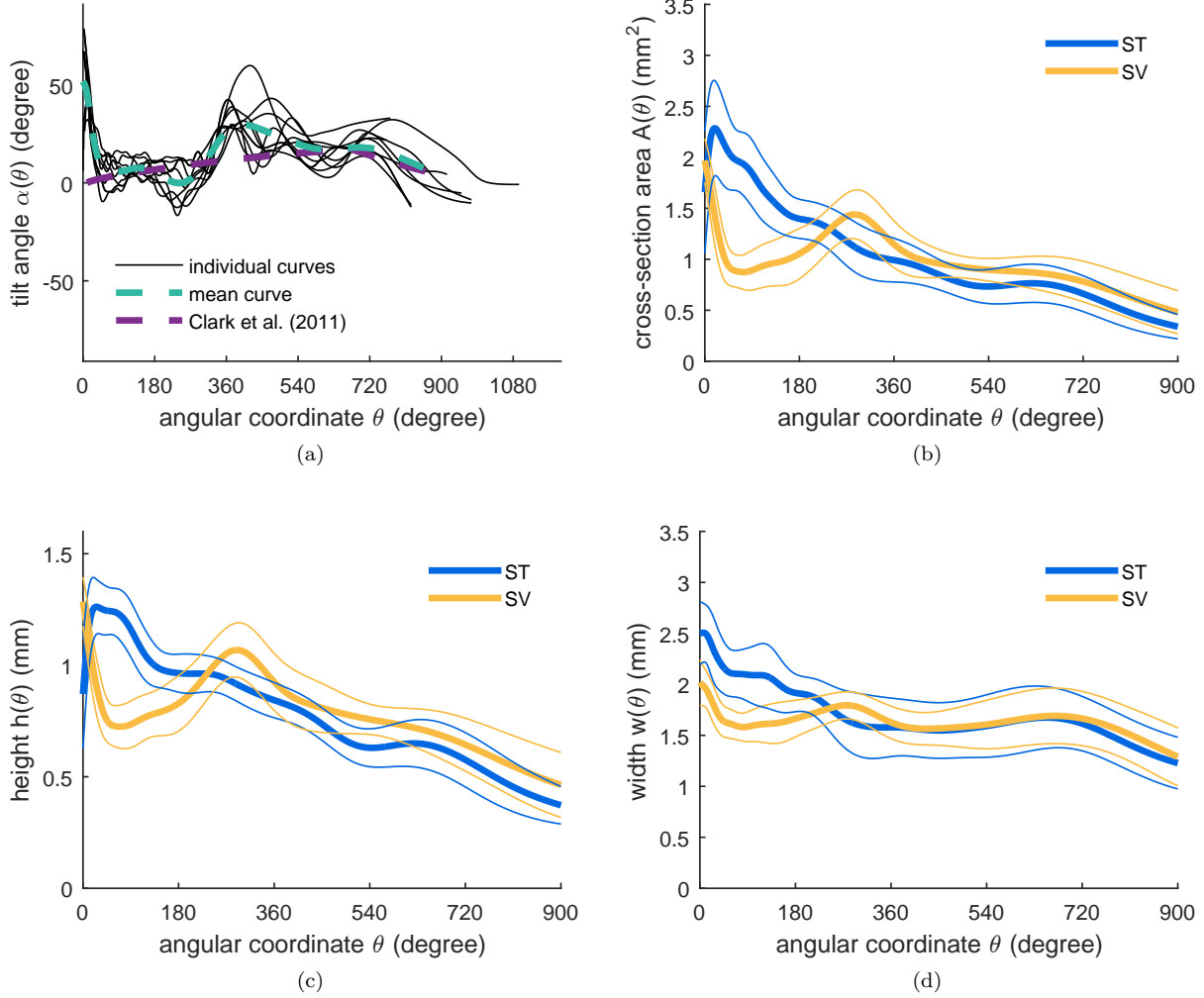


Figure 16: (a) Individual and mean cochlear tilt angle α , the mean angle between $\hat{\mathbf{u}}$ and the major axes of the tympanic and vestibular scalae. Cross-section area (b), heights (c) and widths (d) of the tympanic and vestibular scalae. The thinner lines represent ± 1 standard deviation.

in table 2). Depending on the extraction method chosen, the cochlear central path may be shifted closer to the lateral (as in (Wysocki, 1999; Avcı et al., 2014)) or modiolar wall which would entail again highly different parametrization (see Fig. 9a for the scala tympani). The angular coordinate on the other hand is independent from the centerline. Therefore, as con-

cluded by Verbist et al. (2010) to allow accurate comparisons the angular parametrization should be preferred.

A significant variability is observed for the longitudinal components. The origin chosen for the coordinate system aligns all round windows but not the apexes, whereas the apical coordinate system intro-

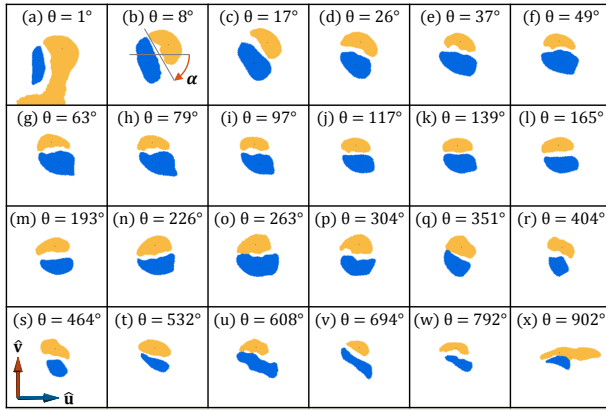


Figure 15: Cross-sections (patient #3), with the scala tympani (blue) and the scala vestibuli (yellow) from the base to the apex. Subfigure (a) illustrates a leakage of the label “scala vestibuli” to the vestibule. Subfigure (x) illustrates the difficulty to have well defined centerlines at the apex, where both scalae merge.

duced by Verbist et al. (2010) would have aligned all apices but not the round windows.

The cochlear moving frame defined in this article allows one to easily measure the profile tilt angle. To our knowledge this paper provides a first quantification of the tilt angle along the full centerline. Clark et al. (2011) introduced this parameter but without any estimation from real data. Their proposed model captures some of the variability (Fig. 16a) but our systematic measurements provide a new insight in the cochlear structure. Gibson et al. (2012) measured the rotation of the osseous spiral lamina in the hook region. The measurements are assessed at four locations (1, 3, 5 and 7 mm distal to the round window) along the basal turn of the cochlea. Slices of MRI images are extracted using an oblique sagittal plane. The acquisition of this plane called Pöschl projection is radiologist-dependent and the rotations measured are difficult to compare with the tilt angle.

The tilt angle measurements shows a relatively repetitive pattern. Close to the round window, the tilt angle is on average greater than 45° . Between 60 and 360° , the tilt angle falls around 0° , making the radial component of the tympanic and vestibular centerlines coincident. This decrease of the tilt an-

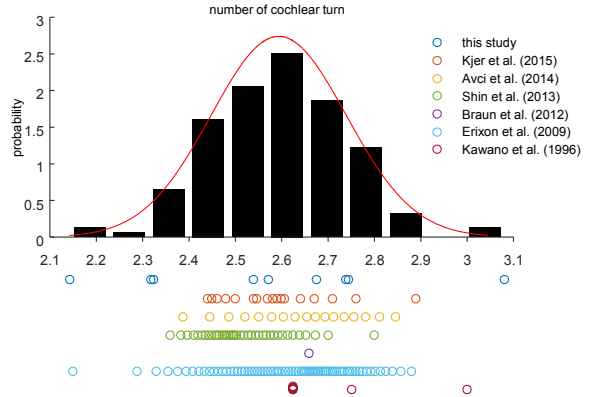


Figure 17: Comparison of measurements of the number of cochlear turns. A normal distribution was fitted to the concatenated measurements.

gle along the basal turn matches with the prominent rotation noted in Gibson et al. (2012)’s study which has been performed between approximately 10 and 100° . After 360° the tilt angle turns positive before becoming flat again at the apex.

Additionally, the cochlear moving frame allows to deduct unambiguously the lateral and the modiolar path from the central one.

4.2. Variability study

When the number of cochlear turns is not specifically detailed (Kawano et al., 1996; Braun et al., 2012; Kjer et al., 2015), many authors transcribed the mean, the standard deviation, the range and the number of the measurements (Erixon et al., 2009; Shin et al., 2013; Avci et al., 2014). For illustration purposes, Fig. 17 shows sets of data values which fulfill the measures listed above (the standard deviation was arbitrarily set to 0.14 for the data in (Erixon et al., 2009)). A normal distribution was fit to the concatenated data. Comparing the results of this current study with previous findings shows that, on one hand the mean number of cochlear turn (2.58) falls extremely close to the mode of the normal distribution (2.59), on the other hand the standard deviation (0.28) is broader than what is found in the literature (0.11 (Kawano et al., 1996), 0.09 (Shin et al.,

2013), 0.17 (Avci et al., 2014)). This result could be explained by the presence of two extreme cases. Patient #5 (2.14) is close the lower end of the range observed by Erixon et al. (2009) (2.15) and according to Jackler et al. (2009)’s classification is not malformed. Cochleae with 3 turns such as the second outlier (3.08) were previously reported by Tian et al. (2006).

Irrespective to the parametrization, our cross-sections measurements are very similar to the ones from Wysocki (1999) and Thorne et al. (1999), our height measurements being also comparable with diameter measurements obtained from inscribed circles (Biedron et al., 2010; Avci et al., 2014). Tympanic cross-section area appears greater to the vestibular one in the basal turn and conversely in the middle and apical turns (as shown in Fig .16b) match with Gulya and Steenerson (1996); Wysocki (1999)’s observations.

The radial component of the different cochlear ducts shows low variability. In accordance with the results from previous studies (Cohen et al., 1996; Baker, 2008), a logarithmic spiral seems to describe well the projected cochlear shape.

The longitudinal component of the cochlea, as described by Verbist et al. (2009), shows a pattern similar to the one in Fig. 10d, which is a decreasing slope, changing to an increasing curve. The “proximal short rising” described by the authors has not been observed in our mean cochlear centerline data but can still be noticed in the mean tympanic and vestibular centerlines. The longitudinal component of the scala tympani was studied by Avci et al. (2014). Unlike Avci et al. (2014) all the scala tympani showed the same profile, which would have been classified as a “rollercoaster” (see subsection 3.2).

Finally, despite the challenge in shape analysis at the apex, the results of this study have the advantage of being meaningful even after the second turn (720°).

4.3. Modiolar axis estimation

The comparison between manual and subsection 3.2 shows that automatically estimated axis is on average slightly further from the axis defined by the experts than the inter- and intra-expert standard deviation. More specifically, the rotation error is similar

to the inter-expert variability while the translation is greater. The variability of the manually defined axes comes from the estimation of the apical axial point rather than the basal axial point. The experts tend to choose a point directly on the centerline rather than at the hypothetical center of the helico-spiral (see Fig. 11b). Theoretically the radius of a logarithmic spiral converges to zero but never reaches it. We can reasonably assume these results can be explained by a bias that occurs with the manual estimation.

Moreover we have shown an example of the influence of a rotation error of 11.5° (Fig. 14), which is of the same order of magnitude as the mean angle error between the automatically and manually estimated axis (10.2°). In some cases the influence is large enough to change the profile of the longitudinal component. For these reasons we can hypothesize that the fact that only one class of Avci et al. (2014)’s classification is found in this study can be explained either by a lack of variability of our database or by the influence of our more reproducible modiolar axis estimation method compared with the manual one.

The comparison between the two estimation methods of the modiolar axis shows that the method of Yoo et al. (2000b) provides a good estimate only when the parameter C_{init} is correctly estimated and when the initialization angle is within a close range of the true value. However, the parameter C_{init} cannot be estimated easily since it depends on the curve discretization and the initial coordinate system. Our method on the other hand is an unbiased estimator of the axis in the absence of noise and does not depend on the choice of an additional extrinsic parameter or the reference frame. Its performance in the presence of noise is fairly similar (up to 2° difference) to the best estimate of Yoo et al. (2000b) and is robust to outliers. Since our approach relies on computing the center of curvature (Eq. B.8 in the supplementary materials), of a noisy centerline, it could be improved by considering scale sensitive discrete curvature computation.

4.4. Implication for cochlear implantation

The preparation and the segmentation of the human cochlea allow us to assess with confidence mean-

ingful information for cochlear implantation and even after the first two basal cochlear turns.

The centerlines of the scala tympani are useful to identify the potential location of insertion trauma. Most longitudinal components show an important “bump” at $184.5^\circ \pm 80.9$ (mean and ± 1 standard deviation), which matches well with the empirical position (around 180°), observed by surgeons, of cochlear trauma and basilar perforation sites (Eshraghi et al., 2003; Wardrop et al., 2005; Nguyen et al., 2012).

In order to make the centerline projections significant, one must pay attention on how to define correctly the cochlear coordinate system.

Fig. 16a shows a distinctive tilt angle, on average greater than 45° close to the round window (as in Fig. 15b). Such a feature may make the electrode array deviate in the scala vestibuli shortly after an insertion through a cochleostomy. The tilt angle may have implication for occurrence of trauma and cochleostomy site selection (Briggs et al., 2009).

Straight electrodes tend to follow the lateral wall of the scala tympani whereas perimodiolar electrodes are designed to follow the modiolar wall. The measure of the lateral, central and modiolar arc lengths (Fig. 9a) could provide, as in (Escudé et al., 2006), information about ideal electrode array length according to the type of electrode and the desired insertion depth.

The height of the scala tympani was measured as the minor axis of the cross-sections, it is also comparable with the diameter of the inscribed circle (subsection 4.2). The results are independent from the cross-section plane orientation. It provides an upper limit for the dimension of an electrode array. We showed (Fig. 16c) that it is of primary importance to have an electrode diameter smaller than 0.5 mm in order to be atraumatic after 360° .

5. Conclusion

We designed an automated method for the cochlear centerline extraction given a segmented cochlea image. A robust method for modiolar axis estimation was developed, validated on a synthetic cochlear model, compared with manual estimation and an-

other algorithm from the literature and finally applied on segmented images of nine temporal bones. Objective geometrical measurement were performed on the tympanic and vestibular duct segmentations assessing, among others, the radial and longitudinal components of the lateral, central and modiolar paths. Cross-section measurements were estimated within a new non-ambiguous moving frame. Close to the round window, the cross-section tilt angle shows an important feature for insertion trauma comprehension. This study was meant to be reproducible and suitable for a larger database in order to improve significantly the knowledge of the cochlea shape variability. Finally, this study could provide the key measurements to validate a parametric shape model of the cochlea and its inner structures. This model could be used to provide prior anatomical information required for analyzing clinical CT images. Indeed due to spatial resolution limitation, conventional CT images alone cannot provide enough fine information about anatomical structures relevant for cochlear implantation (Shin et al., 2013). Specifically the basilar membrane that delimits the scala tympani is nearly invisible with clinically available imaging techniques. Based on the presented results, further studies will analyzed the human cochlear shape variability from large CT image databases.

Acknowledgment

This work was supported by the National Association for Research in Technology (ANRT) through the CIFRE Grant 2013-1165 and Neurelec / Oticon Medical. Part of this work was also funded by the European Research Council through the ERC Advanced Grant MedYMA 2011-291080 (on Biophysical Modeling and Analysis of Dynamic Medical Images).

The authors would like to acknowledge Pr Jacques Darcourt, Dr Philippe R. Franken and Dr Thierry Pourcher of the Nice University’s TIRO team for providing the μ CT images that were used for this study.

- Adunka, O., Unkelbach, M. H., Mack, M., Ham-bek, M., Gstoettner, W., Kiefer, J., Sep. 2004. Cochlear implantation via the round window membrane minimizes trauma to cochlear structures: a histologically controlled insertion study. *Acta Otolaryngol.* 124 (7), 807–12.
- Aschendorff, A., Kromeier, J., Klenzner, T., Laszig, R., Apr. 2007. Quality control after insertion of the nucleus contour and contour advance electrode in adults. *Ear Hear.* 28 (2), 75–79.
- Avci, E., Nauwelaers, T., Lenarz, T., Hamacher, V., Kral, A., Mar. 2014. Variations in microanatomy of the human cochlea. *J. Comp. Neurol.* 00, 1–17.
- Baker, G., 2008. Tracking, modelling and registration of anatomical objects: the human cochlea. Ph.D. thesis, The University of Melbourne.
- Baker, G., Barnes, N., 2004. Principal flow for tubular objects with non-circular cross-sections. In: *Pattern Recognition, 2004. ICPR 2004. Proceedings of the 17th International Conference on.* Vol. 3. IEEE, pp. 750–753.
- Biedron, S., Prescher, A., Ilgner, J., Westhofen, M., Jul. 2010. The internal dimensions of the cochlear scalae with special reference to cochlear electrode insertion trauma. *Otol. Neurotol.* 31 (5), 731–7.
- Braun, K., Böhnke, F., Stark, T., Jun. 2012. Three-dimensional representation of the human cochlea using micro-computed tomography data: presenting an anatomical model for further numerical calculations. *Acta Otolaryngol.* 132 (6), 603–13.
- Briggs, R. J. S., Tykocinski, M., Stidham, K., Rober-son, J. B., jul 2009. Cochleostomy site: Implications for electrode placement and hearing preservation. *Acta Otolaryngol.*
- Buytaert, J. A. N., Salih, W. H. M., Dierick, M., Jacobs, P., Dirckx, J. J. J., 2011. Realistic 3D computer model of the gerbil middle ear, featuring accurate morphology of bone and soft tissue structures. *J. Assoc. Res. Otolaryngol.* 12 (6), 681–696.
- Ceresa, M., Lopez, N. M., Velardo, H. D., Her-rezuelo, N. C., Mistrik, P., Kjer, H. M., Vera, S., Paulsen, R. R., González Ballester, M. Á., 2014. Patient-Specific Simulation of Implant Placement and Function for Cochlear Implantation Surgery Planning. *Med. Image Comput. Comput. Assist. Interv.* 8674, 49–56.
- Clark, J. R., Warren, F. M., Abbott, J. J., 2011. A Scalable Model for Human Scala-Tympani Phantoms. *J. of Med. Device.* 5 (1), 014501.
- Cohen, L. T., Xu, J., Xu, S. A., Clark, G. M., 1996. Improved and simplified methods for specifying positions of the electrode bands of a cochlear implant array. *Am. J. Otol.* 17 (6), 859–865.
- Criminisi, A., Sharp, T., Blake, A., Oct. 2008. GeoS: Geodesic Image Segmentation. *ECCV 10 (1)*, 99–112.
- Dimopoulos, P., Muren, C., Sep. 1990. Anatomic variations of the cochlea and relations to other temporal bone structures. *Acta Radiol.* 31 (5), 439–44.
- Erixon, E., Högstorp, H., Wadin, K., Rask-Andersen, H., Jan. 2009. Variational anatomy of the human cochlea: implications for cochlear implantation. *Otol. Neurotol.* 30 (1), 14–22.
- Escudé, B., James, C., Deguine, O., Cochard, N., Eter, E., Fraysse, B., Jan. 2006. The size of the cochlea and predictions of insertion depth angles for cochlear implant electrodes. *Audiol. Neurotol.* 11 Suppl 1 (suppl 1), 27–33.
- Eshraghi, A. A., Yang, N. W., Balkany, T. J., Mar. 2003. Comparative study of cochlear damage with three perimodiolar electrode designs. *Laryngoscope* 113 (3), 415–9.
- Fayad, J. N., Linthicum, F. H., Aug. 2006. Multi-channel cochlear implants: relation of histopathology to performance. *Laryngoscope* 116 (8), 1310–20.
- Finley, C. C., Holden, T. A., Holden, L. K., Whiting, B. R., Chole, R. A., Neely, G. J., Hullar, T. E., Skinner, M. W., 2008. Role of Electrode Placement

- as a Contributor to Variability in Cochlear Implant Outcomes. *Otol. Neurotol.* 29 (7), 920–928.
- Fowler, D. R., Meinhardt, H., Prusinkiewicz, P., 1992. Modeling seashells. In: *ACM SIGGRAPH Computer Graphics*. Vol. 26. ACM, pp. 379–387.
- Franz, D., Hofer, M., Pfeifle, M., Pirlich, M., Stammering, M., Wittenberg, T., 2014. Wizard-Based Segmentation for Cochlear Implant Planning. In: Deserno, T. M., Handels, H., Meinzer, H.-P., Tolxdorff, T. (Eds.), *Bildverarbeitung für die Medizin 2014 SE - 49*. Informatik aktuell. pp. 258–263.
- Gibson, D., Gluth, M. B., Whyte, A., Atlas, M. D., oct 2012. Rotation of the osseous spiral lamina from the hook region along the basal turn of the cochlea: results of a magnetic resonance image anatomical study using high-resolution DRIVE sequences. *Surg. Radiol. Anat.* 34 (8), 781–5.
- Gulya, A. J., Steenerson, R. L., Feb. 1996. The scala vestibuli for cochlear implantation. An anatomic study. *Arch. Otolaryngol. Head Neck Surg.* 122 (2), 130–132.
- Gunz, P., Ramsier, M., Kuhrig, M., Hublin, J.-J., Spoor, F., Jun. 2012. The mammalian bony labyrinth reconsidered, introducing a comprehensive geometric morphometric approach. *J. Anat.* 220 (6), 529–43.
- Hardy, M., Jan. 1938. The length of the organ of Corti in man. *Am. J. Anat.* 62 (2), 291–311.
- Hatsushika, S.-I., Shepherd, R. K., Tong, Y. C., Clark, G. M., Funasaka, S., Nov. 1990. Dimensions of the Scala Tympani in the Human and Cat with Reference to Cochlear Implants. *Ann. Otol. Rhinol. Laryngol.* 99 (11), 871–876.
- Jackler, R. K., Luxfor, W. M., House, W. F., Oct. 2009. Congenital malformations of the inner ear: A classification based on embryogenesis. *Laryngoscope* 97 (S40), 2–14.
- James, C., Albegger, K., Battmer, R., Burdo, S., Deggouj, N., Deguine, O., Dillier, N., Gersdorff, M., Laszig, R., Lenarz, T., Rodriguez, M. M., Mondain, M., Offeciers, E., Macías, Á. R., Ramsden, R., Sterkers, O., Von Wallenberg, E., Weber, B., Fraysse, B., May 2005. Preservation of residual hearing with cochlear implantation: How and why. *Acta Otolaryngol.* 125 (5), 481–491.
- Kass, M., Witkin, A., Terzopoulos, D., 1988. Snakes: Active contour models. *Int. J. Comput. Vis.* 1 (4), 321–331.
- Kawano, A., Seldon, H. L., Clark, G. M., Sep. 1996. Computer-Aided Three-Dimensional Reconstruction in Human Cochlear Maps: Measurement of the Lengths of Organ of Corti, Outer Wall, Inner Wall, and Rosenthal’s Canal. *Ann. Otol. Rhinol. Laryngol.* 105 (9), 701–709.
- Kjer, H. M., Fagertun, J., Vera, S., Gil, D., González Ballester, M. Á., Paulsen, R. R., Jul. 2015. Free-form image registration of human cochlear μ CT data using skeleton similarity as anatomical prior. *Pattern Recognit. Lett.* 0, 0000.
- Leake, P. A., Hradek, G. T., Snyder, R. L., Oct. 1999. Chronic electrical stimulation by a cochlear implant promotes survival of spiral ganglion neurons after neonatal deafness. *J. Comp. Neurol.* 412 (4), 543–62.
- Liu, C., Rubin, D. B., 1995. ML estimation of the t distribution using EM and its extensions, ECM and ECME. *Stat. Sin.* 5, 19–39.
- Makary, C., Shin, J., Caruso, P., Curtin, H., Merchant, S., Jan. 2010. A histological study of scala communis with radiological implications. *Audiol. Neurotol.* 15 (6), 383–93.
- Meshik, X., Holden, T. A., Chole, R. A., Hullar, T. E., 2010. Optimal cochlear implant insertion vectors. *Otol. Neurotol.* 31 (1), 58–63.
- Nadol, J. B., Sep. 1997. Patterns of neural degeneration in the human cochlea and auditory nerve: Implications for cochlear implantation. *Otolaryngol. Head Neck Surg.* 117 (3), 220–228.
- Nguyen, Y., Miroir, M., Kazmitcheff, G., Sutter, J., Bensidhoum, M., Ferrary, E., Sterkers, O., Bozorg

- Grayeli, A., Jan. 2012. Cochlear implant insertion forces in microdissected human cochlea to evaluate a prototype array. *Audiol. Neurotol.* 17 (5), 290–8.
- Noble, J. H., Labadie, R. F., Majdani, O., Dawant, B. M., Sep. 2011. Automatic segmentation of intra-cochlear anatomy in conventional CT. *IEEE Trans. Biomed. Eng.* 58 (9), 2625–32.
- Perona, P., Malik, J., Jul. 1990. Scale-space and edge detection using anisotropic diffusion. *IEEE Trans. Pattern Anal. Mach. Intell.* 12 (7), 629–639.
- Postnov, A., Zarowski, A., De Clerck, N., Vanpoucke, F., Offeciers, F. E., Van Dyck, D., Peeters, S., May 2006. High resolution micro-CT scanning as an innovative tool for evaluation of the surgical positioning of cochlear implant electrodes. *Acta Otolaryngol.* 126 (5), 467–74.
- Poznyakovskiy, A. A., Zahnert, T., Kalaidzidis, Y., Lazurashvili, N., Schmidt, R., Hardtke, H.-J., Fischer, B., Yarin, Y. M., Dec. 2011. A segmentation method to obtain a complete geometry model of the hearing organ. *Hear. Res.* 282 (1-2), 25–34.
- Poznyakovskiy, A. A., Zahnert, T., Kalaidzidis, Y., Schmidt, R., Fischer, B., Baumgart, J., Yarin, Y. M., Sep. 2008. The creation of geometric three-dimensional models of the inner ear based on micro computer tomography data. *Hear. Res.* 243 (1-2), 95–104.
- Rask-Andersen, H., Erixon, E., Kinnefors, A., Löwenheim, H., Schrott-Fischer, A., Liu, W., May 2011. Anatomy of the human cochlea - implications for cochlear implantation. *Cochlear Implants Int.* 12 (s1), S13–S8.
- Rau, T. S., Würfel, W., Lenarz, T., Majdani, O., Apr. 2013. Three-dimensional histological specimen preparation for accurate imaging and spatial reconstruction of the middle and inner ear. *Int. J. Comput. Assist. Radiol. Surg.* 8 (4), 481–509.
- Reda, F. A., Dawant, B. M., McRackan, T. R., Labadie, R. F., Noble, J. H., 2013. Automatic segmentation of intra-cochlear anatomy in post-implantation ct. In: *SPIE Medical Imaging. International Society for Optics and Photonics*, pp. 86710I–86710I.
- Reda, F. A., McRackan, T. R., Labadie, R. F., Dawant, B. M., Noble, J. H., Feb. 2014a. Automatic segmentation of intra-cochlear anatomy in post-implantation CT of unilateral cochlear implant recipients. *Med. Image Anal.* 18 (3), 605–615.
- Reda, F. A., Noble, J. H., Labadie, R. F., Dawant, B. M., Mar. 2014b. An artifact-robust, shape library-based algorithm for automatic segmentation of inner ear anatomy in post-cochlear-implantation CT. In: *Ourselin, S., Styner, M. A. (Eds.), SPIE Medical Imaging. Vol. 9034. p. 90342V.*
- Schuman, T. A., Noble, J. H., Wright, C. G., Wanna, G. B., Dawant, B. M., Labadie, R. F., Nov. 2010. Anatomic verification of a novel method for precise intrascalar localization of cochlear implant electrodes in adult temporal bones using clinically available computed tomography. *Laryngoscope* 120 (11), 2277–83.
- Shin, K.-J., Lee, J.-Y., Kim, J.-N., Yoo, J.-Y., Shin, C., Song, W.-C., Koh, K.-S., Jul. 2013. Quantitative analysis of the cochlea using three-dimensional reconstruction based on microcomputed tomographic images. *Anat. Rec.* 296 (7), 1083–8.
- Skinner, M. W., Ketten, D. R., Holden, L. K., Harding, G. W., Smith, P. G., Gates, G. A., Neely, J. G., Kletzker, G. R., Brunsdon, B., Blocker, B., Sep. 2002. CT-derived estimation of cochlear morphology and electrode array position in relation to word recognition in Nucleus-22 recipients. *J. Assoc. Res. Otolaryngol.* 3 (3), 332–50.
- Stakhovskaya, O., Sridhar, D., Bonham, B. H., Leake, P. A., 2007. Frequency map for the human cochlear spiral ganglion: Implications for cochlear implants. *J. Assoc. Res. Otolaryngol.* 8 (2), 220–233.

- Thorne, M., Salt, A. N., DeMott, J. E., Henson, M. M., Henson, O. W., Gewalt, S. L., Oct. 1999. Cochlear fluid space dimensions for six species derived from reconstructions of three-dimensional magnetic resonance images. *Laryngoscope* 109 (10), 1661–8.
- Tian, Q., Linthicum, F. H., Fayad, J. N., May 2006. Human cochleae with three turns: an unreported malformation. *Laryngoscope* 116 (5), 800–3.
- van der Marel, K. S., Briaire, J. J., Wolterbeek, R., Snel-Bongers, J., Verbist, B. M., Frijns, J. H. M., Jan. 2014. Diversity in cochlear morphology and its influence on cochlear implant electrode position. *Ear and Hearing* 35 (1), e9–20.
- Verbist, B. M., Ferrarini, L., Briaire, J. J., Zarowski, A., Admiraal-behloul, F., Olofsen, H., Reiber, J. H. C., Frijns, J. H. M., Jun. 2009. Anatomic considerations of cochlear morphology and its implications for insertion trauma in cochlear implant surgery. *Otol. Neurotol.* 30 (4), 471–7.
- Verbist, B. M., Skinner, M. W., Cohen, L. T., Leake, P. A., James, C., Boëx, C., Holden, T. A., Finley, C. C., Roland, P. S., Roland, J. T., Haller, M., Patrick, J. F., Jolly, C. N., Faltys, M. A., Briaire, J. J., Frijns, J. H. M., Jul. 2010. Consensus panel on a cochlear coordinate system applicable in histologic, physiologic, and radiologic studies of the human cochlea. *Otol. Neurotol.* 31 (5), 722–30.
- Viergever, M. A., Oct. 1978. Basilar membrane motion in a spiral-shaped cochlea. *J. Acoust. Soc. Am.* 64 (4), 1048.
- Wardrop, P., Whinney, D., Rebscher, S. J., Roland, J. T., Luxford, W., Leake, P. A., May 2005. A temporal bone study of insertion trauma and intracochlear position of cochlear implant electrodes. I: Comparison of Nucleus banded and Nucleus *Contour*TM electrodes. *Hear. Res.* 203 (1-2), 54–67.
- Wright, C. G., Roland, P. S., 2005. Temporal bone microdissection for anatomic study of cochlear implant electrodes. *Cochlear Implants Int.* 6 (4), 159–168.
- Wysocki, J., 1999. Dimensions of the human vestibular and tympanic scalae. *Hear. Res.* 135 (1-2), 39–46.
- Xianfen, D., Siping, C., Changhong, L., Yuanmei, W., 2005. 3d semi-automatic segmentation of the cochlea and inner ear. In: *Engineering in Medicine and Biology Society, 2005. IEEE-EMBS 2005. 27th Annual International Conference of the IEEE*, pp. 6285–6288.
- Xu, H. X., Kim, G. H., Snissarenko, E. P., Cureoglu, S., Paparella, M. M., May 2012. Multi-channel cochlear implant histopathology: are fewer spiral ganglion cells really related to better clinical performance? *Acta Otolaryngol.* 132 (5), 482–90.
- Xu, J., Xu, S. A., Cohen, L. T., Clark, G. M., Jan. 2000. Cochlear view: postoperative radiography for cochlear implantation. *Am. J. Otol.* 21 (1), 49–56.
- Yoo, S. K., Wang, G., Rubinstein, J. T., Skinner, M. W., Vannier, M. W., Jun. 2000a. Three-dimensional modeling and visualization of the cochlea on the Internet. *IEEE Trans. Inf. Technol. Biomed.* 4 (2), 144–51.
- Yoo, S. K., Wang, G., Rubinstein, J. T., Vannier, M. W., Oct. 2000b. Three-dimensional geometric modeling of the cochlea using helico-spiral approximation. *IEEE Trans. Biomed. Eng.* 47 (10), 1392–402.
- Zrunek, M., Lischka, M., 1981. Dimensions of the scala vestibuli and sectional areas of both scales. *Arch. Otorhinolaryngol.* 233 (4151), 99–104.
- Zrunek, M., Lischka, M., Hochmair-Desoyer, I., Burian, K., 1980. Dimensions of the scala tympani in relation to the diameters of multichannel electrodes. *Arch. Otorhinolaryngol.* 229, 159–165.